COMMUNICATIONS IN COMPUTATIONAL PHYSICS
Vol. **4**, No. 5, pp. 1008-1024

Commun. Comput. Phys.
November 2008

A Third Order Conservative Lagrangian Type Scheme on Curvilinear Meshes for the Compressible Euler Equations†

Juan Cheng[1,*] and Chi-Wang Shu[2]

[1] *Institute of Applied Physics and Computational Mathematics, Beijing 100088, China.*
[2] *Division of Applied Mathematics, Brown University, Providence, RI 02912, USA.*

Received 10 February 2008; Accepted (in revised version) 1 March 2008

Available online 8 July 2008

Abstract. Based on the high order essentially non-oscillatory (ENO) Lagrangian type scheme on quadrilateral meshes presented in our earlier work [3], in this paper we develop a third order conservative Lagrangian type scheme on curvilinear meshes for solving the Euler equations of compressible gas dynamics. The main purpose of this work is to demonstrate our claim in [3] that the accuracy degeneracy phenomenon observed for the high order Lagrangian type scheme is due to the error from the quadrilateral mesh with straight-line edges, which restricts the accuracy of the resulting scheme to at most second order. The accuracy test given in this paper shows that the third order Lagrangian type scheme can actually obtain uniformly third order accuracy even on distorted meshes by using curvilinear meshes. Numerical examples are also presented to verify the performance of the third order scheme on curvilinear meshes in terms of resolution for discontinuities and non-oscillatory properties.

AMS subject classifications: 65M99

Key words: Lagrangian type scheme, high order accuracy, conservative scheme, curvilinear mesh, WENO reconstruction, compressible Euler equations.

1 Introduction

In numerical simulations of multidimensional fluid flow, there are two typical choices: a Lagrangian framework, in which the mesh moves with the local fluid velocity, and an Eulerian framework, in which the fluid flows through a grid fixed in space. More

†Dedicated to Professor Xiantu He on the occasion of his 70th birthday.
*Corresponding author. *Email addresses:* cheng_juan@iapcm.ac.cn (J. Cheng), shu@dam.brown.edu (C.-W. Shu)

generally, the motion of the grid can also be chosen arbitrarily, this method is called the Arbitrary Lagrangian-Eulerian method (ALE; see, e.g., [1,7,14]).

Lagrangian methods are widely used in many fields for multi-material flow simulations such as astrophysics and computational fluid dynamics (CFD), due to their distinguished advantage of being able to capture the material interface sharply. In the past years, many efforts have been made to develop Lagrangian methods. Some algorithms are developed from the nonconservative form of the Euler equations, see, e.g., [10,13,22], while others start from the conservative form of the Euler equations, e.g. those in [1,4,11,12].

In our previous paper [3], we developed a class of Lagrangian type schemes on quadrilateral meshes for solving the Euler equations which are based on the high order essentially non-oscillatory (ENO) reconstruction. Advantages for the schemes in [3] include their conservativity for the density, momentum and total energy, their essentially non-oscillatory performance, parameter-free implementation, and their formal high order accuracy both in space and time. However, we also found that our third order Lagrangian type scheme could only achieve second order accuracy on two dimensional distorted Lagrangian meshes. We attributed this phenomenon to a fundamental problem in the formulation of the Lagrangian schemes. Since in a Lagrangian simulation, each cell represents a material particle, its shape may change with the movement of fluid. Therefore, a cell with an initially quadrilateral shape may not keep its shape as a quadrilateral at a later time. It usually becomes a curved quadrilateral. Thus if during our Lagrangian simulation the mesh is always kept as quadrilateral with straight-line edges, this approximation of the mesh will bring second order error into the scheme. Finally we made a conclusion that for a Lagrangian type scheme in multi-dimensions, it can be at most second order accurate if curved meshes are not used. Meanwhile, we also predicted that our scheme can be extended to higher than second order accuracy if curvilinear meshes are used. In this paper, we explore curvilinear meshes to demonstrate our claim stated above. We will develop a third order scheme on curved quadrilateral meshes in two space dimensions. The reconstruction is based on the high order WENO procedure [8,9] but with simpler linear weights. The accuracy test and some non-oscillatory tests are presented to verify our claim. The scheme can also be extended to higher than third order accuracy if a higher order approximation is used on both the meshes and the discretization of the governing equations.

An outline of the rest of this paper is as follows. In Section 2, we describe the individual steps of the third order Lagrangian type scheme on curvilinear meshes in two space dimensions. In Section 3, numerical examples are given to verify the performance of the new Lagrangian type method. In Section 4 we will give concluding remarks.

2 The third order conservative Lagrangian type scheme on curvilinear meshes

2.1 The compressible Euler equations in Lagrangian formulation

The Euler equations for unsteady compressible flow in the reference frame of a moving control volume can be expressed in the integral form in the Cartesian coordinates as

$$\frac{d}{dt}\int_{\Omega(t)}\mathbf{U}d\Omega+\int_{\Gamma(t)}\mathbf{F}d\Gamma=0, \tag{2.1}$$

where $\Omega(t)$ is the moving control volume enclosed by its boundary $\Gamma(t)$. The vector of the conserved variables $\mathbf{U}$ and the flux vector $\mathbf{F}$ are given by

$$\mathbf{U}=\begin{pmatrix}\rho\\ \mathbf{M}\\ E\end{pmatrix},\qquad \mathbf{F}=\begin{pmatrix}(\mathbf{u}-\dot{\mathbf{x}})\cdot\mathbf{n}\rho\\ (\mathbf{u}-\dot{\mathbf{x}})\cdot\mathbf{n}\mathbf{M}+p\mathbf{n}\\ (\mathbf{u}-\dot{\mathbf{x}})\cdot\mathbf{n}E+p\mathbf{u}\cdot\mathbf{n}\end{pmatrix}, \tag{2.2}$$

where ρ is the density, $\mathbf{u}$ is the velocity, $\mathbf{M}=\rho\mathbf{u}$ is the momentum, E is the total energy and p is the pressure, $\dot{\mathbf{x}}$ is the velocity of the control volume boundary $\Gamma(t)$, $\mathbf{n}$ denotes the unit outward normal to $\Gamma(t)$. The system (2.1) represents the conservation of mass, momentum and energy.

The set of equations is completed by the addition of an equation of state (EOS) with the following general form

$$p=p(\rho,e), \tag{2.3}$$

where $e=E/\rho-\frac{1}{2}|\mathbf{u}|^2$ is the specific internal energy. Especially, if we consider the ideal gas, then the equation of state has a simpler form,

$$p=(\gamma-1)\rho e,$$

where γ is a constant representing the ratio of specific heat capacities of the fluid.

This paper focuses on solving the governing equations (2.1)-(2.2) in a Lagrangian framework, in which it is assumed that $\dot{\mathbf{x}}=\mathbf{u}$, and the vectors $\mathbf{U}$ and $\mathbf{F}$ then take the simpler form

$$\mathbf{U}=\begin{pmatrix}\rho\\ \mathbf{M}\\ E\end{pmatrix},\qquad \mathbf{F}=\begin{pmatrix}0\\ p\mathbf{n}\\ p\mathbf{u}\cdot\mathbf{n}\end{pmatrix}. \tag{2.4}$$

2.2 The third order conservative Lagrangian type scheme on curvilinear meshes in two space dimension

The 2D spatial domain Ω is discretized into $N_x\times N_y$ computational cells. $I_{i+1/2,j+1/2}$ is a generalized quadrilateral cell, with each edge being a quadratic curve. This curved quadrilateral cell is uniquely identified by its four vertices $\{(x_{i,j},y_{i,j}),$ $(x_{i+1,j},y_{i+1,j}),$ $(x_{i+1,j+1},$ $y_{i+1,j+1}),$ $(x_{i,j+1},y_{i,j+1})\}$ and the four middle points of its four quadratic edges $\{(x_{i+1/2,j},$ $y_{i+1/2,j}),$ $(x_{i+1,j+1/2},$ $y_{i+1,j+1/2}),$ $(x_{i+1/2,j+1},y_{i+1/2,j+1}),$ $(x_{i,j+1/2},y_{i,j+1/2})\}$. $S_{i+1/2,j+1/2}$ denotes the area of the cell $I_{i+1/2,j+1/2}$ with $i=1,\cdots,N_x,$

$j=1,\cdots,N_y$. For a given cell $I_{i+1/2,j+1/2}$, the location of the cell center is denoted by $(x_{i+1/2,j+1/2},y_{i+1/2,j+1/2})$. The fluid velocity $(u_{i,j},v_{i,j})$ is defined at the vertex of the mesh and $(u_{i+1/2,j},v_{i+1/2,j}),(u_{i,j+1/2},v_{i,j+1/2})$ define the fluid velocities at the middle points of the curvilinear edges of the cell. We consider only the non-staggered mesh, with all the variables except velocity stored at the cell center of $I_{i+1/2,j+1/2}$ in the form of cell averages. For example, the values of the cell averages for the cell $I_{i+1/2,j+1/2}$ denoted by $\overline{\rho}_{i+1/2,j+1/2}$, $\overline{M}^x_{i+1/2,j+1/2}$, $\overline{M}^y_{i+1/2,j+1/2}$ and $\overline{E}_{i+1/2,j+1/2}$ are defined as follows

$$\begin{aligned}
\overline{\rho}_{i+1/2,j+1/2}&=\frac{1}{S_{i+1/2,j+1/2}}\iint_{I_{i+1/2,j+1/2}}\rho dxdy,\\
\overline{M}^x_{i+1/2,j+1/2}&=\frac{1}{S_{i+1/2,j+1/2}}\iint_{I_{i+1/2,j+1/2}}M_x dxdy,\\
\overline{M}^y_{i+1/2,j+1/2}&=\frac{1}{S_{i+1/2,j+1/2}}\iint_{I_{i+1/2,j+1/2}}M_y dxdy,\\
\overline{E}_{i+1/2,j+1/2}&=\frac{1}{S_{i+1/2,j+1/2}}\iint_{I_{i+1/2,j+1/2}}E dxdy,
\end{aligned}$$

where ρ, M_x, M_y and E are the density, x-momentum, y-momentum and total energy, respectively.

2.2.1 Spatial and time discretizations

The conservative semi-discrete scheme for Eqs. (2.1) and (2.4) has the following form on the 2D non-staggered mesh

$$\begin{aligned}
&\frac{d}{dt}\begin{pmatrix}\overline{\rho}_{i+1/2,j+1/2}S_{i+1/2,j+1/2}\\ \overline{M}^x_{i+1/2,j+1/2}S_{i+1/2,j+1/2}\\ \overline{M}^y_{i+1/2,j+1/2}S_{i+1/2,j+1/2}\\ \overline{E}_{i+1/2,j+1/2}S_{i+1/2,j+1/2}\end{pmatrix}\\
&=-\int_{\partial I_{i+1/2,j+1/2}}\hat{\mathbf{F}}dl=-\int_{\partial I_{i+1/2,j+1/2}}\begin{pmatrix}\hat{f}_D(\mathbf{U}_n^-,\mathbf{U}_n^+)\\ \hat{f}_{M_x}(\mathbf{U}_n^-,\mathbf{U}_n^+)\\ \hat{f}_{M_y}(\mathbf{U}_n^-,\mathbf{U}_n^+)\\ \hat{f}_E(\mathbf{U}_n^-,\mathbf{U}_n^+)\end{pmatrix}dl.
\end{aligned}\tag{2.5}$$

Here $\mathbf{U}^{\pm}=(\rho^{\pm},M_x^{\pm},M_y^{\pm},E^{\pm})$ are the values of mass, x-momentum, y-momentum and total energy at two sides of the boundary. $\mathbf{U}_n^{\pm}=(\rho^{\pm},M_n^{\pm},E^{\pm})$, where $M_n^{\pm}$ are the left and right component values of the momentum which is normal to the cell boundary, i.e. $M_n^{\pm}=(M_x^{\pm},M_y^{\pm})\cdot\mathbf{n}$. $\hat{f}_D$, $\hat{f}_{M_x}$, $\hat{f}_{M_y}$ and $\hat{f}_E$ are the numerical fluxes of mass, x-momentum, y-momentum and total energy across the cell boundary respectively. Here in the La-

grangian formulation, we have

$$\begin{cases} \hat{f}_D(\mathbf{U}_n,\mathbf{U}_n)=0, \\ \hat{f}_{M_x}(\mathbf{U}_n,\mathbf{U}_n)=pn_x, \\ \hat{f}_{M_y}(\mathbf{U}_n,\mathbf{U}_n)=pn_y, \\ \hat{f}_E(\mathbf{U}_n,\mathbf{U}_n)=pu_n, \end{cases} \tag{2.6}$$

where $u_n=\mathbf{u}\cdot\mathbf{n}$ is the normal velocity at the cell boundary.

Similar to [3], we use the high order WENO reconstruction with Roe-type characteristic decomposition [21] to obtain $\mathbf{U}^{\pm}$ and $\mathbf{U}_n^{\pm}$ at the boundary and also use sufficiently high order quadrature to construct schemes up to the expected third-order spatial accuracy. The Dukowicz flux [5] and the Lax-Friedrichs (L-F) flux are used in this paper for numerical tests. To save space, in the following we will only list the difference in the procedure of constructing the scheme on the curved quadrilateral meshes from that on the straight-line edged quadrilateral meshes. We refer to [3] for the other details.

Since calculating the integral of the numerical flux and determining the reconstruction polynomials in the scheme (2.5) involve the integration on each curved quadrilateral cell, firstly we should know the accurate description of each curvilinear cell with quadratically-curved edges by the information of the coordinates of its four vertices and the four middle points of its four edges. We accomplish this procedure by a mapping from a canonical square to a curved quadrilateral cell. For simplicity, here we denote the coordinates of the four vertices of the concerned cell as $\{(x_m,y_m),m=1,2,3,4\}$, $\{(\xi_m,\eta_m),m=1,2,3,4\}$ and the middle points of its four edges as $\{(x_{12},y_{12}),\ (x_{23},y_{23}),\ (x_{34},y_{34}),\ (x_{41},y_{41})\}$, $\{(\xi_{12},\eta_{12}),\ (\xi_{23},\eta_{23}),\ (\xi_{34},\eta_{34}),\ (\xi_{41},\eta_{41})\}$ in the (x,y)-plane and (ξ,η)-plane respectively (see Fig. 1). Then the shape of this curvilinear cell can be determined by the following interpolation function:

$$\begin{aligned} x&=\sum_{m=1}^{4}\varphi_m x_m+\sum_{n=m+1\,(mod4)}\varphi_{mn}x_{mn}, \\ y&=\sum_{m=1}^{4}\varphi_m y_m+\sum_{n=m+1\,(mod4)}\varphi_{mn}y_{mn}, \end{aligned} \tag{2.7}$$

where

$$\begin{aligned} &\varphi_m=-\frac{1}{4}(1+\xi_m\xi)(1+\eta_m\eta)(1-\xi_m\xi-\eta_m\eta), \quad m=1,2,3,4, \\ &\varphi_{mn}=\frac{1}{2}(1+\xi_{mn}\xi+\eta_{mn}\eta)(1-\xi_{mn}^2\eta^2-\eta_{mn}^2\xi^2), \quad n=m+1\,(mod4),\ -1\le\xi,\ \eta\le 1. \end{aligned}$$

For each boundary edge Γ_m of the 4 curved edges in $\partial I_{i+1/2,j+1/2}$, the curvilinear integral

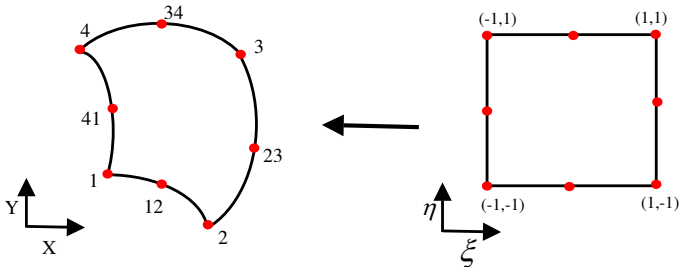

Figure 1: Mapping from a canonical square to a curved quadrilateral with quadratically-curved edges.

of the numerical flux $\hat{\mathbf{F}}$ is discretized by a 3-point Gaussian quadrature,

$$\begin{aligned}\int_{\Gamma_m}\hat{\mathbf{F}}dl &= \int_{-1}^{1}\hat{\mathbf{F}}\sqrt{\left(\frac{dx}{d\zeta}\right)^2+\left(\frac{dy}{d\zeta}\right)^2}d\zeta \\ &\approx \sum_{k=1}^{3}\omega_k\hat{\mathbf{F}}(\mathbf{U}_n(G_k))\sqrt{\left(\frac{dx}{d\zeta}\right)^2(G_k)+\left(\frac{dy}{d\zeta}\right)^2(G_k)},\end{aligned} \tag{2.8}$$

where $\zeta=\xi$ if the edge Γ_m corresponds to a ξ line, $\zeta=\eta$ if the edge Γ_m corresponds to an η line. $G_k=-1,0,1$ are the Gaussian quadrature (Simpson's rule) points at this edge. $\{\omega_k,k=1,3\}$ are the weights with the values of $1/3,4/3,1/3$ respectively.

The integral of the reconstruction polynomial $p(x,y)$ on the curved quadrilateral cell can be computed in the (ξ,η) coordinates for example by a 4×4-point Gaussian integration formula

$$\begin{aligned}\int_{I_{i+1/2,j+1/2}}p(x,y)dxdy &= \int_{-1}^{1}\int_{-1}^{1}p(x,y)|J|d\xi d\eta \\ &\approx \sum_{k,l=1}^{4}\omega_k\omega_l p(G_{k,l})|J(G_{k,l})|,\end{aligned} \tag{2.9}$$

where J is the Jacobian matrix, $G_{k,l}=(\xi(k),\eta(l))$ are the Gaussian quadrature points of the cell in the (ξ,η)-plane with $\xi(1)=\eta(1)=-1$, $\xi(2)=\eta(2)=-\frac{\sqrt{5}}{5}$, $\xi(3)=\eta(3)=\frac{\sqrt{5}}{5}$, $\xi(4)=\eta(4)=1$, and $\{\omega_k,k=1,4\}$ are the weights which have the values $\omega_1=\frac{1}{6}$, $\omega_2=\frac{5}{6}$, $\omega_3=\frac{5}{6}$, $\omega_4=\frac{1}{6}$.

The procedure of choosing the candidate stencils for a third order WENO reconstruction in our framework is discussed in detail in [2], in the context of remapping. Briefly described, we start from the family of candidate stencils for the second-order approximation, and determine the smoothest stencil for the linear reconstruction in the cell $I_{i+1/2,j+1/2}$, for example the smoothest stencil might consist of Cell '0' (i.e. $I_{i+1/2,j+1/2}$), Cell '1', and Cell '2', see Fig. 2. Extending from these three cells, we can then choose the following three sets of stencils which come from different directions for the third order reconstruction in Cell '0',

$$\{A:0,1,2,3,4,6\},\quad \{B:0,1,2,5,8,9\},\quad \{C:0,1,2,7,8,12\}.$$

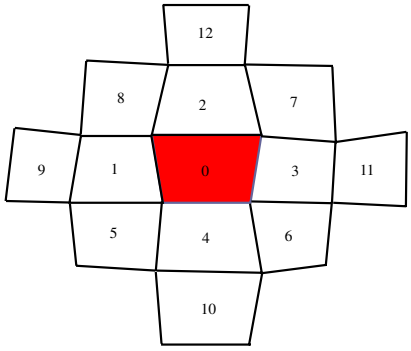

Figure 2: The potential cells for the candidate stencils.

Among these stencils, we can see Stencil A represents a central stencil and the other two are biased stencils.

The ENO procedure in [3], which chooses one stencil out of the candidates mentioned above based on the local smoothness of the solution, can be used to obtain our third order reconstructions. However, our computational experience indicates that accuracy degeneracy and even occasional instability might develop, because the stencil chosen might correspond to a linearly unstable one too often. We refer to [15,17] for more details of this phenomenon. Although the introduction of a biasing factor into the ENO procedure to favor the central or upwind linearly stable stencil will help to resolve this problem [2,17], we have found through our numerical experiments that the following simple WENO procedure is more robust.

The WENO procedure here is similar to that in [3] except that different weights are used. In this procedure, the coefficients of the reconstruction polynomial are chosen as the weighted averages of those determined by the above final three possible stencils. Here we use different weights to make our third order scheme on curved meshes more stable. To be specific, we use density as an example. To determine the coefficients $\{a_{mn}, m+n\leq 2\}$ of the quadratic polynomial reconstruction function inside the cell $I_{i+1/2,j+1/2}$,

$$\rho_{i+1/2,j+1/2}(x,y)=\sum_{m+n\leq 2} a_{mn}(x-x_{i+1/2,j+1/2})^m(y-y_{i+1/2,j+1/2})^n,$$

suppose the coefficients of the reconstruction polynomials of the three candidate stencils are $a^i_{mn}, i=1,2,3$, then we choose $a_{mn}=\sum_{i=1}^3 w^i a^i_{mn}$ where the weights w^i are chosen as

$$w^i=\frac{\tilde{w}^i}{\sum_{j=1}^3 \tilde{w}^j}, \qquad \tilde{w}^j=\frac{c_j}{\sum_{1\leq m+n\leq 2}(S_D)^{m+n-1}|a^j_{mn}|^2+\epsilon}, \tag{2.10}$$

where c_j are the linear weights, S_D is the total area of the computational domain which is introduced to preserve the self-similarity property of the reconstruction, and we typically

choose $\epsilon = 10^{-6}$. In order to improve the linear stability of the scheme, we choose $c_1 = 2$ to increase the linear weight of the central stencil A in the reconstruction and $c_2 = c_3 = 1$ for the other two stencils. This crude WENO reconstruction, which does not theoretically increase the accuracy of each candidate stencil but is very easy to compute, performs nicely in our numerical experiments. We refer the readers to the review paper [19] for more details regarding various types of WENO schemes and the mechanism to design nonlinear weights for achieving accuracy and non-oscillatory performance. The advantage and disadvantage of the way we have chosen the linear weights here are discussed in Section 2.3.3 in [19].

We also use the third order TVD Runge-Kutta method [20] for the time discretization of the scheme, see [3] for the implementation details.

2.2.2 The determination of the velocity

The vertex velocity of the mesh is determined in the same way as in [3]. For the velocity of an edge's middle point, the tangential velocity is defined as the arithmetic average of the tangential velocities from its two sides. As to the normal velocity, for the Dukowicz flux, we obtain it as a by-product of the approximate Riemann solver and for the L-F flux, we obtain it by a Roe average of the normal velocities from its two sides.

In our numerical non-oscillatory tests, we found that the velocity at the middle point of an edge should be limited in order to avoid the edge from dramatic curving, which may lead to a degeneracy of the cell (i.e. different sides of the cell intersect each other inside). We perform the limitation on the movement of the middle point as described below, which does not destroy the formal accuracy of the numerical scheme.

We first set a reference circular arc for each curvilinear edge which is on the same side of the line connecting the two end-points of the edge. The reference circular arc is determined by the two end-points of the edge and another point which is preset at the normal direction of the above mentioned line from its middle point. The distance between this point and the middle point of the line is as follows,

$$d = c\Delta l^2, \tag{2.11}$$

where Δl is the straight-line length of the edge, c is a parameter which can be used to determine the allowed amplitude of the circular arc. For the edge with two fixed end points, if c is larger, then the radius of the reference circular arc (we call it as the reference curvature radius) is smaller, and vice versa. After we obtain the new position of the related points at each Runge-Kutta time step, we check the curvature radius of the curvilinear edge at its middle point. If it is less than its pre-set reference curvature radius, we move this middle point to the location of the middle point of the pre-set reference circular arc. We can control the extent of this modification by choosing an adequate pre-set c. In particular, we remark that any choice of $c > 0$ will not destroy the asymptotic formal accuracy when the solution is smooth, as a Taylor expansion indicates that the actual curvature radius for a smooth solution corresponds to a distance d in (2.11) of the size $\mathcal{O}(\Delta l^3)$, which

is asymptotically smaller than $c\Delta l^2$ with any $c>0$, hence the limiter is never enacted for smooth solutions and small enough Δl. This is verified numerically in our accuracy test in next section.

3 Numerical results in two space dimensions

In this section, in the accuracy test we will only show the results obtained by the Dukowicz flux because the results by other fluxes introduced in [3] are quite similar. In the non-oscillatory tests, we will show the results obtained by the Dukowicz flux and the L-F flux.

3.1 Accuracy test

Here we choose the two-dimensional vortex evolution problem [18] for our accuracy test. The vortex problem is described as follows: The mean flow is $\rho=1$, $p=1$ and $(u,v)=(1,1)$ (diagonal flow). We add to this mean flow an isentropic vortex perturbations in (u,v) and the temperature $T=p/\rho$, no perturbation in the entropy $S=p/\rho^\gamma$.

$$(\delta u,\delta v)=\frac{\epsilon}{2\pi}e^{0.5(1-r^2)}(-\overline{y},\overline{x}),\qquad \delta T=-\frac{(\gamma-1)\epsilon^2}{8\gamma\pi^2}e^{(1-r^2)},\qquad \delta S=0,$$

where $(-\overline{y},\overline{x})=(x-5,y-5)$, $r^2=\overline{x}^2+\overline{y}^2$, and the vortex strength is $\epsilon=5$.

The computational domain is taken as $[0,10]\times[0,10]$, and periodic boundary conditions are used. In this test, the Courant number is chosen as 0.5 and the parameter c in (2.11) for the limitation on the movement of the middle points at the cell edges is set to be 0.4.

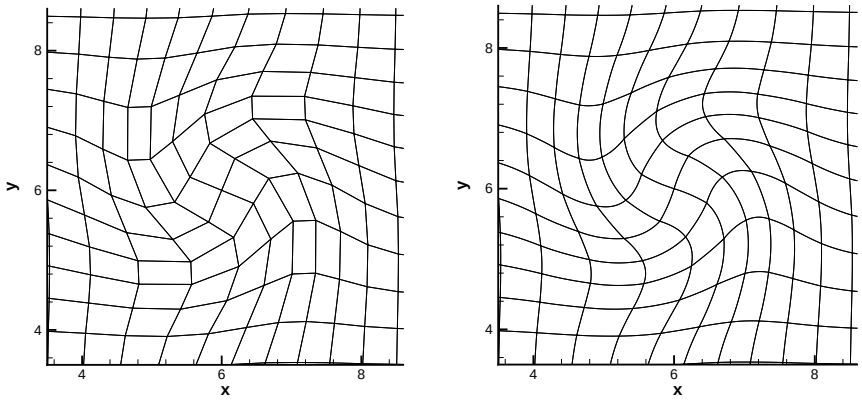

Figure 3: The local mesh of the vortex problem at $t=1$. Left: quadrilateral; Right: curved quadrilateral.

For comparison, we compute the third order scheme with the Dukowicz flux and the above mentioned WENO reconstruction both on the straight-line edged quadrilateral meshes and the curved quadrilateral meshes. Fig. 3 shows the local meshes simulated by

Table 1: Errors of the third order scheme on 2D straight-line edged quadrilateral meshes for the vortex problem using $N_x \times N_y$ initially uniform mesh cells.

$N_x = N_y$	Norm	Density	order	Momentum	order	Energy	order
20	L_1	0.31E-2		0.56E-2		0.11E-1	
	L_∞	0.29E-1		0.50E-1		0.16E+0	
40	L_1	0.77E-3	2.00	0.14E-2	2.05	0.28E-2	2.03
	L_∞	0.94E-2	1.64	0.19E-1	1.39	0.55E-1	1.55
80	L_1	0.19E-3	2.05	0.32E-3	2.07	0.67E-3	2.06
	L_∞	0.23E-2	2.04	0.46E-2	2.06	0.12E-1	2.17
160	L_1	0.45E-4	2.03	0.79E-4	2.03	0.16E-3	2.04
	L_∞	0.58E-3	1.98	0.11E-2	2.09	0.27E-2	2.19

Table 2: Errors of the third order scheme on 2D curved quadrilateral meshes for the vortex problem using $N_x \times N_y$ initially uniform mesh cells.

$N_x = N_y$	Norm	Density	order	Momentum	order	Energy	order
20	L_1	0.14E-2		0.31E-2		0.63E-2	
	L_∞	0.12E-1		0.28E-1		0.70E-1	
40	L_1	0.20E-3	2.81	0.48E-3	2.73	0.90E-3	2.81
	L_∞	0.33E-2	1.89	0.75E-2	1.89	0.21E-1	1.71
80	L_1	0.26E-4	2.93	0.60E-4	2.98	0.11E-3	2.98
	L_∞	0.58E-3	2.49	0.12E-2	2.63	0.35E-2	2.59
160	L_1	0.35E-5	2.91	0.80E-5	2.91	0.15E-4	2.95
	L_∞	0.12E-3	2.26	0.22E-3	2.43	0.66E-3	2.41

these two kinds of schemes at $t = 1$. The convergence results at $t = 1$ are listed in Tables 1-2 respectively. In Table 1, we can only see second order accuracy just as the result in [3], while in Table 2 we can see the desired third order accuracy at least in the L_1 norm which verifies our claim.

We also study the convergence property of our algorithm on a non-uniform initial mesh which is obtained by performing a random perturbation with the amplitude of ten percent of the mesh size along both x and y directions to each inner node of the above used uniform initial mesh. The convergence results of our scheme by using this kind of non-uniform initial mesh are shown in Tables 3-4. We can see that the result on the curved meshes here is similar to that with the uniform initial mesh while the result on the straight-line edged meshes using the non-uniform initial mesh is worse than that using the uniform initial mesh, especially in the L_∞ norm.

Remark 3.1. In fact, we have also experimented with another type of WENO reconstruction described below: Denote the Cell '0' to be $I_{i+1/2,j+1/2}$, then we choose four central stencils and four biased stencils for our WENO reconstruction from the information on the cell '0' and its 12 neighboring cells (see Fig. 2). The stencils we use are as follows:

Table 3: Errors of the third order scheme on 2D straight-line edged quadrilateral meshes for the vortex problem using $N_x \times N_y$ initially non-uniform mesh cells.

$N_x = N_y$	Norm	Density	order	Momentum	order	Energy	order
20	L_1	0.31E-2		0.57E-2		0.11E-1	
	L_∞	0.31E-1		0.57E-1		0.15E+0	
40	L_1	0.82E-3	1.90	0.14E-2	2.00	0.28E-2	1.98
	L_∞	0.10E-1	1.60	0.21E-1	1.45	0.57E-1	1.35
80	L_1	0.23E-3	1.83	0.38E-3	1.89	0.70E-3	2.02
	L_∞	0.34E-2	1.61	0.65E-2	1.67	0.13E-1	2.20
160	L_1	0.78E-4	1.55	0.12E-3	1.62	0.18E-3	1.92
	L_∞	0.22E-2	0.65	0.29E-2	1.15	0.60E-2	1.05

Table 4: Errors of the third order scheme on 2D curved quadrilateral meshes for the vortex problem using $N_x \times N_y$ initially non-uniform mesh cells.

$N_x = N_y$	Norm	Density	order	Momentum	order	Energy	order
20	L_1	0.15E-2		0.32E-2		0.63E-2	
	L_∞	0.15E-1		0.28E-1		0.73E-1	
40	L_1	0.20E-3	2.84	0.48E-3	2.75	0.90E-3	2.80
	L_∞	0.35E-2	2.15	0.74E-2	1.93	0.20E-1	1.88
80	L_1	0.26E-4	2.94	0.60E-4	2.99	0.11E-3	2.98
	L_∞	0.63E-3	2.47	0.12E-2	2.62	0.35E-2	2.50
160	L_1	0.35E-5	2.91	0.81E-5	2.90	0.15E-4	2.95
	L_∞	0.12E-3	2.34	0.21E-3	2.55	0.64E-3	2.45

Central stencils:

$$\{0,1,2,3,4,5\}, \quad \{0,1,2,3,4,6\}, \quad \{0,1,2,3,4,7\}, \quad \{0,1,2,3,4,8\},$$

Biased stencils:

$$\{0,1,2,8,9,12\}, \quad \{0,1,4,5,9,10\}, \quad \{0,3,4,6,10,11\}, \quad \{0,2,3,7,11,12\}.$$

We can obtain eight reconstruction polynomials from these eight stencils. Then the final nonlinear WENO reconstruction polynomial is obtained by a combination of these eight polynomials by using similar smoothness indicators and nonlinear weights as those in Hu and Shu [8]. To be more specific, we define the following smoothness indicator to measure the smoothness.

$$SI = \sum_{1 \le |\alpha| \le 2} \int_{I_{i+1/2,j+1/2}} |S_{i+1/2,j+1/2}|^{|\alpha|-1} (D^\alpha p(x,y))^2 dxdy \tag{3.1}$$

where α is a multi-index and D is the derivative operator, for example, when $\alpha = (1,1)$

Table 5: Errors of the third order scheme in the Remark 3.1 on 2D straight-line edged quadrilateral meshes for the vortex problem using $N_x \times N_y$ initially uniform mesh cells.

$N_x = N_y$	Norm	Density	order	Momentum	order	Energy	order
20	L_1	0.31E-2		0.56E-2		0.12E-1	
	L_∞	0.30E-1		0.41E-1		0.13E+0	
40	L_1	0.73E-3	2.10	0.13E-2	2.13	0.27E-2	2.20
	L_∞	0.82E-2	1.86	0.13E-1	1.60	0.41E-1	1.67
80	L_1	0.18E-3	2.04	0.31E-3	2.04	0.64E-3	2.07
	L_∞	0.18E-2	2.18	0.36E-2	1.89	0.98E-2	2.06
160	L_1	0.45E-4	2.00	0.77E-4	2.01	0.16E-3	2.01
	L_∞	0.45E-3	2.02	0.91E-3	1.99	0.24E-2	2.04

Table 6: Errors of the third order scheme in the Remark 3.1 on 2D curved quadrilateral meshes for the vortex problem using $N_x \times N_y$ initially uniform mesh cells.

$N_x = N_y$	Norm	Density	order	Momentum	order	Energy	order
20	L_1	0.14E-2		0.30E-2		0.58E-2	
	L_∞	0.11E-1		0.30E-1		0.64E-1	
40	L_1	0.11E-3	3.71	0.25E-3	3.54	0.47E-3	3.63
	L_∞	0.13E-2	3.14	0.32E-2	3.23	0.75E-2	3.10
80	L_1	0.60E-5	4.16	0.16E-4	4.01	0.27E-4	4.12
	L_∞	0.75E-4	4.12	0.21E-3	3.95	0.51E-3	3.88
160	L_1	0.39E-6	3.93	0.10E-5	3.92	0.17E-5	4.02
	L_∞	0.61E-5	3.61	0.14E-4	3.91	0.36E-4	3.82

then $|\alpha| = 2$ and $D^\alpha p(x,y) = \partial p^2(x,y)/\partial x \partial y$. The nonlinear weights are then defined as

$$\omega_k = \frac{\tilde{\omega}_k}{\sum_l \tilde{\omega}_l}, \qquad \tilde{\omega}_l = \frac{c_l}{(\epsilon + SI_l)^2} \tag{3.2}$$

where $\{c_l, l = 1,8\}$ are the linear weights. Here we set $c_l = 2$ for the central stencils and $c_l = 1$ for the biased stencils. Tables 5-6 contain the error results of the third order code with this WENO reconstruction on the straight-line edged quadrilateral meshes and the curved quadrilateral meshes respectively. We can see our third order scheme on the curved meshes can yield higher than third order accuracy for all the concerned quantities both in the L_1 norm and in the L_∞ norm while the corresponding scheme on the quadrilateral meshes still only achieves second order accuracy. These accuracy results reinforce our claim on the reason of the accuracy degeneracy problem in the Lagrangian type scheme being on the quadrilateral meshes with straight-line edges.

Unfortunately, we also find out that the smoothness indicator (3.1)-(3.2), which is developed mainly for the regular Eulerian meshes, does not seem to perform well in the Lagrangian type scheme framework when simulating problems with strong discontinu-

ities which cause meshes to generate severe aspect ratios and distortions. It seems that a new way to measure smoothness taking the mesh distortion and large aspect ratios into account is necessary, however we will not perform such an investigation in this paper. In the following non-oscillatory tests, we apply the WENO reconstruction introduced in the previous section rather than the WENO reconstruction in this remark.

3.2 Non-oscillatory tests

We test our third order scheme on two examples with discontinuous solutions. The purpose here is to assess the non-oscillatory property of the scheme, rather than to show any advantage of higher order schemes. In fact for such test cases with strong shocks and relatively simple solution structure, high order schemes have very little advantage over a good first or second order scheme.

Example 3.1. (The Saltzman problem [6]).

We solve the Euler equations (2.1)-(2.4), with γ=5/3, in the initial region $[0,1]\times[0,0.1]$. The left end of the computational box is a piston, which moves to the right with a constant velocity of 1.0. The initial mesh, shown in Fig. 4, is 100 cells in the x-direction and 10 cells in the y-direction, defined by

$$x(i,j)=(i-1)\Delta x+(11-j)\sin(0.01\pi(i-1))\Delta y, \qquad y(i,j)=(j-1)\Delta y$$

where $\Delta x=\Delta y=0.01$. We note that the initial mesh is deliberately distorted to set it as a more demanding test case. The initial condition is a stationary gas with a unity density and an internal energy of 10^{-4}. Reflective boundary conditions are used on the right, upper and lower boundaries.

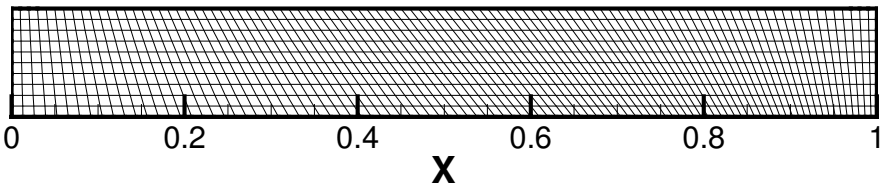

Figure 4: The initial mesh of the Saltzman problem.

For this test case, it is necessary to first use a smaller Courant number in order to maintain stability. The Courant number λ is set to be 0.01 initially and returns to be 0.5 after $t=0.01$. We perform the limitation on the movement of the middle points at the cell edges by choosing the parameter $c=0.4$ in (2.11). By the analytical shock relation, the post shock density is 4.0 and the shock speed is 1.333. The third order Lagrangian numerical results for the Dukowicz flux and the L-F flux are shown in Figs. 5-6 for the time $t=0.6$ respectively, corresponding to an analytical shock location at $x=0.8$. We can observe that our third order scheme preserves one-dimensional solution well except for the region near the top and bottom wall boundaries where the result is affected by the

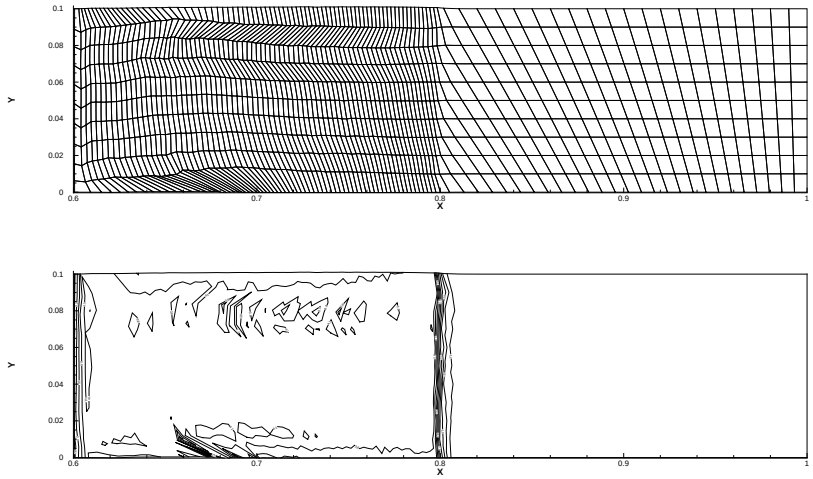

Figure 5: The result of the Saltzman problem with the Dukowicz flux at $t=0.6$. Top: mesh; Bottom: density contour plots from 1.2 to 4.8 with 12 equally spaced contours.

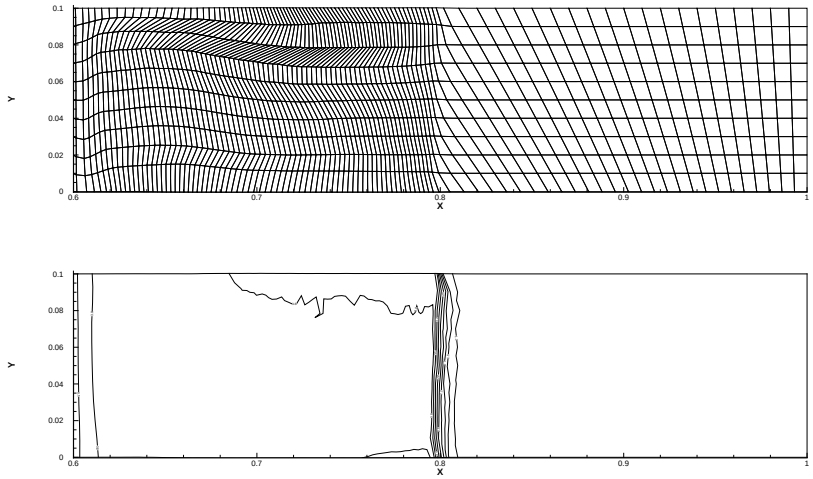

Figure 6: The result of the Saltzman problem with the L-F flux at $t=0.6$. Top: mesh; Bottom: density contour plots from 1.2 to 4.8 with 12 equally spaced contours.

boundary conditions. Fig. 7 shows the density results with both fluxes along the line $y=0.05$ at $t=0.6$. Notice that, because of the grid distortion, the grid points are not on this line and interpolation must be used to plot these cuts. Comparing with the exact solution, we can see our simulation solutions are essentially non-oscillatory. The slight post-shock oscillation is mainly due to the Lagrangian framework and distorted meshes, and is present also for lower order simulations.

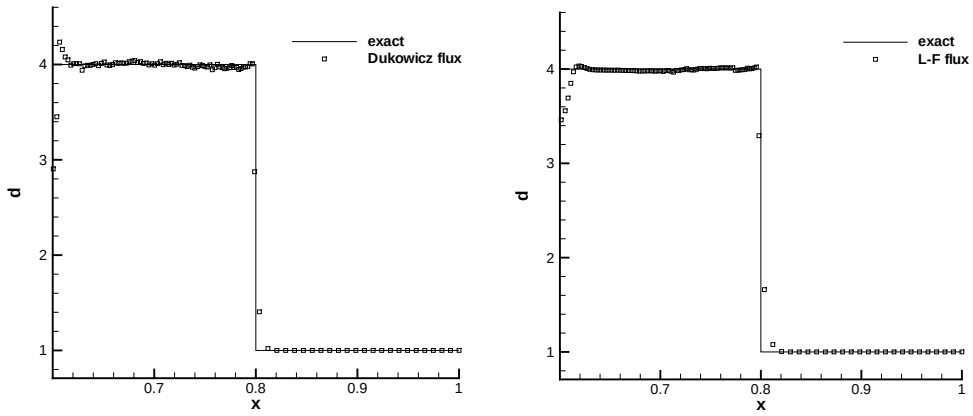

Figure 7: The density results of the Saltzman problem along the line $y=0.05$ at $t=0.6$. The solid line is the exact solution. Left: the Dukowicz flux; Right: the L-F flux.

Example 3.2. (The Sedov blast wave problem [16])

This example is the Sedov blast wave problem in a Cartesian coordinate system. It models the expanding wave by an intense explosion in a perfect gas. The solution is radial symmetric, however the simulation is performed on a Cartesian grid in order to assess the stability and symmetry property of the scheme. The initial uniform grid consists of 30×30 rectangular cells with a total edge length of 1.1 in both directions. The initial condition is set to have unity density and zero velocity, and also to have zero specific internal energy except in the first zone, where it has a value of 182.09. The analytical solution gives a shock at radius unity at time unity with a peak density of 6. In this test, the Courant number λ is set to be 0.5. The parameter c in (2.11) for the limitation on the movement of the middle points at the cell edges is chosen as 0.2. Figs. 8-9 show the results by the third order Lagrangian calculations with the Dukowicz flux and the L-F flux at the time $t=1$ respectively.

4 Concluding remarks

In this paper we have developed a third order Lagrangian type scheme on the curved quadrilateral meshes for solving Euler equations which are based on high order weighted essentially non-oscillatory (WENO) reconstruction. This work is aimed to demonstrate our claim in [3] where we attributed the accuracy degeneracy phenomenon observed in the third order Lagrangian type scheme to the error from the quadrilateral meshes with straight-line edges. Similar to the scheme on the quadrilateral meshes introduced in [3], the scheme on the curved quadrilateral meshes is conservative for density, momentum and total energy, are essentially non-oscillatory, and have no parameters to be tuned for individual test cases. Besides, it can actually obtain the desired third order accuracy by using the curvilinear meshes. Some accuracy and non-oscillatory tests are provided to verify that the scheme achieves the designed third order accuracy and can also simu-

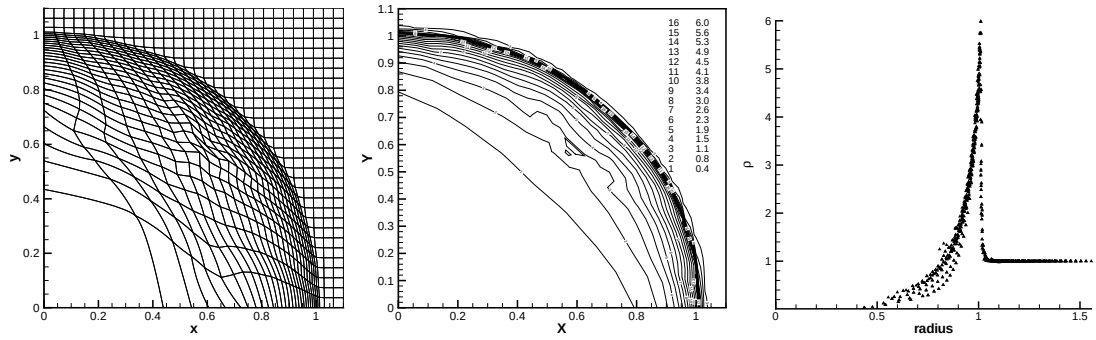

Figure 8: The Sedov problem with Dukowicz flux at $t=1$. Left: the mesh; Middle: density contours; Right: density as a function of the radius.

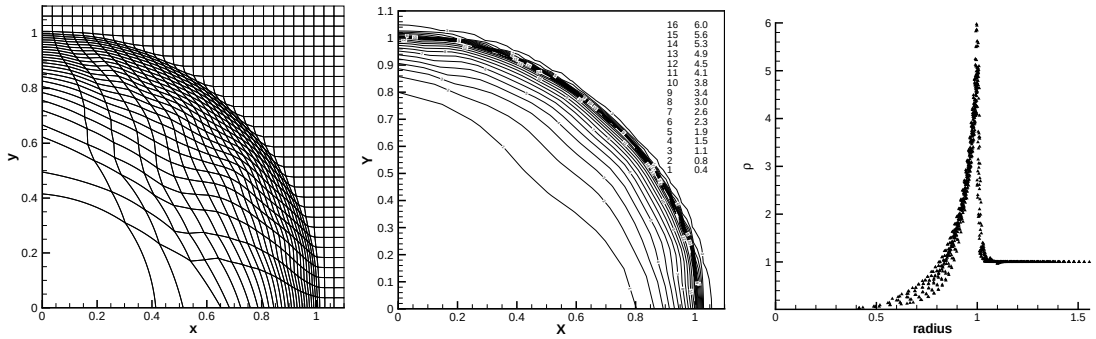

Figure 9: The Sedov problem with L-F flux at $t=1$. Left: the mesh; Middle: density contours; Right: density as a function of the radius.

late problems containing discontinuities. In future work we will study new smoothness indicators in the WENO reconstruction, which take the mesh distortion and large aspect ratios into consideration, in order to improve the robustness of the high order Lagrangian type schemes for shock calculations.

Acknowledgments

The research of the first author is supported in part by NSFC grant 10572028. Additional support is provided by the National Basic Research Program of China under grant 2005CB321702, by the Foundation of National Key Laboratory of Computational Physics under grant 9140C6902010603 and by the National Hi-Tech Inertial Confinement Fusion Committee of China. The research of the second author is supported in part by NSF grant DMS-0510345.

References

[1] D.J. Benson, Computational methods in Lagrangian and Eulerian hydrocodes, Comput. Method. Appl. Mech. Eng., 99 (1992), 235-394.

[2] J. Cheng and C.-W. Shu, A high order accurate conservative remapping method on staggered meshes, Appl. Numer. Math., 58 (2008), 1042-1060.
[3] J. Cheng and C.-W. Shu, A high order ENO conservative Lagrangian type scheme for the compressible Euler equations, J. Comput. Phys., 227 (2007), 1567-1596.
[4] B. Després and C. Mazeran, Lagrangian gas dynamics in two dimensions and lagrangian systems, Arch. Rational Mech. Anal., 178 (2005), 327-372.
[5] J.K. Dukowicz, A general, non-iterative Riemann solver for Godunov method, J. Comput. Phys., 61 (1985), 119-137.
[6] J.K. Dukowicz and B.J.A. Meltz, Vorticity errors in multidimensional Lagrangian codes, J. Comput. Phys., 99 (1992), 115-134.
[7] C. Hirt, A. Amsden and J. Cook, An arbitrary Lagrangian-Eulerian computing method for all flow speeds, J. Comput. Phys., 14 (1974), 227-253.
[8] C. Hu and C.-W. Shu, Weighted essentially non-oscillatory schemes on triangular meshes, J. Comput. Phys., 150 (1999), 97-127.
[9] G. Jiang and C.-W. Shu, Efficient implementation of weighted ENO schemes, J. Comput. Phys., 126 (1996), 202-228.
[10] R. Loubère and M.J. Shashkov, A subcell remapping method on staggered polygonal grids for arbitrary-Lagrangian-Eulerian methods, J. Comput. Phys., 209, 2005, 105-138.
[11] P.-H. Maire, R. Abgrall, J. Breil and J. Ovadia, A cell-centered Lagrangian scheme for two-dimensional compressible flow problems, SIAM J. Sci. Comput., 29 (2007), 1781-1824.
[12] C.D. Munz, On Godunov-type schemes for Lagrangian gas dynamics, SIAM J. Numer. Anal., 31 (1994), 17-42.
[13] J. von Neumann and R.D. Richtmyer, A method for the calculation of hydrodynamics shocks, J. Appl. Phys., 21 (1950), 232-237.
[14] J.S. Peery and D.E. Carroll, Multi-material ALE methods in unstructured grids, Comput. Method. Appl. Mech. Eng., 187 (2000), 591-619.
[15] A. Rogerson and E. Meiberg, A numerical study of the convergence properties of ENO schemes, J. Sci. Comput., 5 (1990), 151-167.
[16] L.I. Sedov, Similarity and Dimensional Methods in Mechanics, Academic Press, New York, 1959.
[17] C.-W. Shu, Numerical experiments on the accuracy of ENO and Modified ENO schemes, J. Sci. Comput., 5 (1990), 127-149.
[18] C.-W. Shu, Essentially non-oscillatory and weighted essentially non-oscillatory schemes for hyperbolic conservation laws, in "Advanced Numerical Approximation of Nonlinear Hyperbolic Equations", B. Cockburn, C. Johnson, C.-W. Shu and E. Tadmor (Editor: A. Quarteroni), Lecture Notes in Mathematics, volume 1697, Springer, Berlin, 1998, 325-432.
[19] C.-W. Shu, High order weighted essentially non-oscillatory schemes for convection dominated problems, SIAM Rev., to appear.
[20] C.-W. Shu and S. Osher, Efficient implementation of essentially non-oscillatory shock-capturing schemes, J. Comput. Phys., 77 (1988), 439-471.
[21] C.-W. Shu, T.A. Zang, G. Erlebacher, D. Whitaker and S. Osher, High-order ENO schemes applied to two- and three-dimensional compressible flow, Appl. Numer. Math., 9, 1992, 45-71.
[22] P.R. Woodward and P. Colella, The numerical simulation of two-dimensional fluid flow with strong shocks, J. Comput. Phys., 54 (1984), 115-173.